Magnetic neutron scattering of thermally quenched K-Co-Fe Prussian blue analog photomagnet

Daniel M. Pajerowski,[1,2] V. Ovidiu Garlea,[3] Elisabeth S. Knowles,[2] Matthew J. Andrus,[4] Matthieu F. Dumont,[2,4] Yitzi M. Calm,[2] Stephen E. Nagler,[3] Xin Tong,[5] Daniel R. Talham,[4] and Mark W. Meisel[2]

[1]*NIST Center for Neutron Research, Gaithersburg, Maryland 20899-6012, USA*

[2]*Department of Physics and National High Magnetic Field Laboratory, University of Florida, Gainesville, Florida 32611-8440, USA*

[3]*Quantum Condensed Matter Division, Oak Ridge National Laboratory, Oak Ridge, Tennessee 37831-6393, USA*

[4]*Department of Chemistry, University of Florida, Gainesville, Florida 32611-7200, USA*

[5]*Instrument and Source Design Division, Oak Ridge National Laboratory, Oak Ridge, Tennessee 37831-6393, USA*

(Received 7 June 2012; published 20 August 2012)

Magnetic order in the thermally quenched photomagnetic Prussian blue analog coordination polymer $K_{0.27}Co[Fe(CN)_6]_{0.73}[D_2O_6]_{0.27}\cdot 1.42D_2O$ has been studied down to 4 K with unpolarized and polarized neutron powder diffraction as a function of applied magnetic field. Analysis of the data allows the on-site coherent magnetization of the Co and Fe spins to be established. Specifically, magnetic fields of 1 and 4 T induce moments parallel to the applied field, and the sample behaves as a ferromagnet with a wandering axis.

DOI: 10.1103/PhysRevB.86.054431 PACS number(s): 75.50.Xx, 75.25.−j, 75.30.Gw, 75.50.Lk

I. INTRODUCTION

Manipulating magnetization with photons is now a major research focus because it may yield materials capable of dense information storage. An epitomic example of a photomagnetic coordination polymer is potassium cobalt hexacyanoferrate, $K_\alpha Co[Fe(CN)_6]_\beta\cdot nH_2O$ (from now on referred to as Co-Fe, with the crystal structure shown in Fig. 1), which displays magnetic order and an optical charge transfer induced spin transition (CTIST).[1] The details of the magnetism in Co-Fe have been investigated with bulk probes such as magnetization[2] and ac susceptibility,[3] as well as atomic level probes such as x-ray magnetic circular dichroism (XMCD)[4] and muon spin relaxation (μ-SR).[5] However, we utilize neutron scattering because it is capable of extracting the magnetic structure, including the length and direction of the magnetic moments associated with different crystallographic positions.

Neutron scattering research has been important in understanding the structure of materials similar to Co-Fe. For example, neutron diffraction has been used to elucidate the location of water molecules, to identify the long-range magnetic order, and to explore the spin delocalization in Prussian blue.[6–8] Later work used similar techniques to investigate hydrogen adsorption in $Cu_3[Co(CN)_6]_2$, along with vibrational spectroscopy,[9] and neutron vibrational spectroscopy was also measured in $Zn_3[Fe(CN)_6]_2$.[10] Likewise, magnetic structure determination with neutrons was used to explore negative magnetization in $Cu_{0.73}Mn_{0.77}[Fe(CN)_6]\cdot nH_2O$,[11] and to extract on-site moments in Berlin green[12,13] and in $(Ni_xMn_{1-x})_3[Cr(CN)_6]_2$ molecule-based magnets.[14]

To this end, we have performed neutron powder diffraction (NPD) on deuterated Co-Fe samples in magnetic states resulting from thermal quenching. Briefly, at room temperature, the photomagnetic Co-Fe with optimal iron vacancies is paramagnetic, with a transition to the diamagnetic low-spin state when cooling below nominally 200 K. It is below 100 K that applied light may convert molecules from diamagnetic to paramagnetic and back, and below around 20 K where this effect is most striking due to the large susceptibility of the magnetically ordered state. However, a magnetically ordered state may also be achieved at low temperatures by thermally quenching,[15,16] where the paramagnetic 300 K state is cooled so quickly to below 100 K that it does not relax to the diamagnetic ground state. It is this magnetic, thermally quenched state that we study with NPD as a function of magnetic field, while complementary magnetization, transmission electron microscopy (TEM), Fourier transform infrared spectroscopy (FT-IR), and elemental analysis have also been performed on the sample. We find that Co-Fe possesses a correlated spin glass ground state that is driven via magnetic field to behave as a ferromagnet with a wandering axis.

II. EXPERIMENTAL DETAILS

A. Synthesis

To begin preparation of $K_\alpha Co[Fe(CN)_6]_\beta\cdot nD_2O$ powder,[17] a 75 ml solution of 0.1 mol/l KNO_3 in D_2O was added to a 75 ml solution of 20 $\times 10^{-3}$ mol/l $K_3[Fe(CN)_6]$ in D_2O, and stirred for 10 min. While continuing to stir, a 300 ml solution of 5×10^{-3} mol/l $CoCl_2$ in D_2O was added dropwise over the course of 2 h. Stirring of the final solution was allowed to continue 2 additional hours subsequent to complete mixing. Next, the precipitate was collected by centrifugation at 2000 rpm (210 rad/s) for 10 min (600 s) and dried under vacuum. This procedure was repeated 14 times until 4.37 g of powder was collected. Potassium ferricyanide, anhydrous cobalt chloride, and potassium nitrate were all purchased from Sigma-Aldrich. To remove water, the potassium nitrate was heated in an oven to 110 °C (383 K) for 4 h before use. All other reagents and chemicals were used without further purification. Deuterium oxide was purchased from Cambridge Isotope Laboratories, Inc.

B. Instrumentation

Neutron powder-diffraction experiments were conducted using the HB2A diffractometer at the High Flux Isotope Reactor[18] using the Ge[113] monochromator with $\lambda =$ 2.41 Å (0.241 nm). Sample environment on HB2A utilized an Oxford 5 T, vertical-field magnet with helium cryogenics. Neutron polarization was achieved with a ^{3}He cell that produced 79% polarization at the beginning of the experiment

 ©2012 American Physical Society

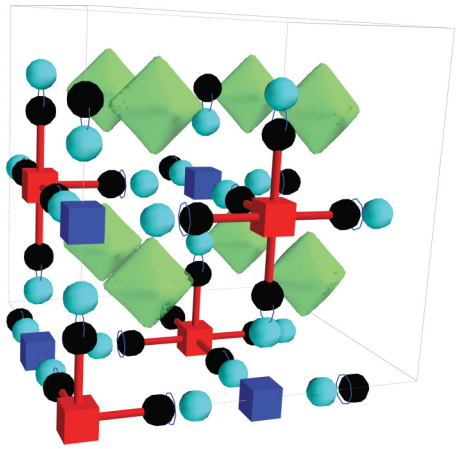

FIG. 1. (Color online) Co-Fe unit cell. Crystallographic positions of atoms within the unit cell are illustrated for Co (blue cubes), Fe (red cubes), Fe-C bonds (red tubes), C (black spheres), N (cyan spheres), coordinated D_2O positions (blue circles), and interstitial D_2O (green contoured isosurfaces), while K ions within the cages cannot be seen in this figure due to masking from D_2O isosurfaces. Details of structure determination are presented in Sec. III.

and decayed to 63% polarization after 20 h at the end of the experiment, to give an average polarization of 71% for both up and down polarization measurements, and we did not perform polarization analysis after the sample but instead followed established methods for powder diffraction with polarized neutrons.[19,20] The flipping difference spectra were obtained by subtracting the diffraction data, measured with the incident neutron polarization parallel to the applied field and magnetization, from the data recorded with the incident polarization antiparallel to the field. Magnetic measurements were performed using a Quantum Design MPMS XL superconducting quantum interference device (SQUID) magnetometer. Infrared spectra were recorded on a Thermo Scientific Nicolet 6700 spectrometer. Energy dispersive x-ray spectroscopy (EDS) and TEM were conducted on a JEOL 2010F superprobe by the Major Analytical Instrumentation Center at the University of Florida (UF). The UF Spectroscopic Services Laboratory performed combustion analysis.

C. Analysis preparations

For NPD, 4.37 g of powder were mounted in a cylindrical aluminum can. Thermal quenching to trap the magnetic state was achieved by filling the cryostat bath with liquid helium and directly inserting a sample stick from ambient temperature. To avoid hydrogen impurities, the powder was wetted with deuterium oxide, and to avoid sample movement in magnetic fields, an aluminum plug was inserted above the sample. To measure magnetization, samples heavier than 10 mg were mounted in gelcaps and held in plastic straws. Thermal quenching in the SQUID was achieved by equilibrating the cryostat to 100 K, and directly inserting the sample stick from ambient temperature. For measurements in 10 mT, samples are cooled through the ordering temperature in 10 mT, and for 1 and 4 T measurements there is no observed thermal hysteresis. For FT-IR, less than 1 mg amounts of sample were suspended in an acetone solution, deposited on KBr salt plates, and allowed to dry. For EDS and TEM, acetone suspensions of the powder were deposited onto 400 mesh copper grids with an ultrathin carbon film on a holey carbon support obtained from Ted Pella, Inc.

D. Diffraction analysis scheme

Intensities were fit to the standard powder diffraction equation with a correction for absorption,[21]

$$I(\theta) = A_0 \frac{m_{hkl}|F(hkl)|^2}{\sin\theta\ \sin 2\theta}\ \eta(\theta), \tag{1}$$

with

$$\eta(\theta) = e^{-(1.713-0.037\sin^2\theta)\mu R+(0.093+0.375\sin^2\theta)\mu^2 R^2}, \tag{2}$$

where A_0 is an overall scale factor, m_{hkl} is the multiplicity of the scattering vector, F is the structure factor, θ is the scattering angle, μ is the linear attenuation coefficient, and R is the radius of the sample cylinder. For our sample and experimental arrangement $\mu R = 0.17$, which has little effect on the observed intensities aside from scale. The structure factor has nuclear (F_N) and magnetic (F_M) contributions, and for unpolarized neutrons

$$|F|^2 = |F_N + F_M|^2 = |F_N|^2 + |F_M|^2. \tag{3}$$

On the other hand, F_N and F_M can coherently interfere for polarized neutrons such that, for moments collinear with P,

$$|F|^2 = |F_N + F_M|^2 = |F_N|^2 + |F_M|^2 \pm 2PF_NF_M, \tag{4}$$

where P is the neutron polarization fraction and the sign of the final term depends upon up or down neutron polarization.[21] For nuclear scattering,

$$F_N(hkl) = \sum_j n_j b_j e^{iG\cdot d_j} e^{-W_j}, \tag{5}$$

where the sum is over all atoms in the unit cell, n is related to the average occupancy, b is the coherent nuclear scattering length, G is the hkl dependent reciprocal lattice vector, d is the direct space atomic position, and $W = BQ^2/16\pi^2$ is the Debye-Waller factor. For magnetic scattering, all coherent scattering is modeled to be along the applied field, which is perpendicular to the scattering plane, so that

$$F_M(hkl) = \frac{\gamma r_0}{2} \sum_j m_j(Q) e^{iG\cdot d_j} e^{-W_j}, \tag{6}$$

where $\frac{\gamma r_0}{2} = 2.695$ fm, and the magnetization can be written as

$$\begin{aligned} m_j(Q) &= \langle L_z\rangle_j f_{L,j}(Q) + 2\langle S_z\rangle_j f_{S,j}(Q) \\ &= g_{J,j}\langle J_z\rangle_j f_{J,j}(Q) \\ &= \langle J_z\rangle_j [g_{L,j} f_{L,j}(Q) + g_{S,j} f_{S,j}(Q)], \end{aligned} \tag{7}$$

where $\langle J_z\rangle$ is the average total angular momentum, $\langle L_z\rangle$ is the average orbital angular momentum, $\langle S_z\rangle$ is the average spin angular momentum, $f_J(Q)$ is the magnetic form factor for the total angular momentum, $f_L(Q)$ is the magnetic form factor for the orbital angular momentum, $f_S(Q)$ is the magnetic form factor for the spin angular momentum, and g_J, g_L, and g_S may be determined by Wigner's formula.[22] The tabulated form factor values within the dipole approximation are used

for the spin and orbital form factors.[23] Squared differences between observed and calculated intensities were minimized using a Nelder-Mead simplex algorithm. Open-source Python 2.7 libraries were utilized to aid in plotting routines, matplotlib 1.0.1 and Mayavi2, and computation, NumPy 1.6.1 and SciPy 0.7.2. Reported uncertainties of fit parameters are the square root of the diagonal terms in the covariance matrix multiplied by the standard deviation of the residuals.

III. RESULTS AND ANALYSES

The synthesis of Co-Fe with heavy water to reduce incoherent neutron scattering does not alter the documented magnetic properties (Fig. 2). Bistable Co-Fe is paramagnetic at room temperature and has a diamagnetic ground state at low temperatures. The paramagnetic state can be trapped by rapid cooling to yield the quenched state, which shows magnetic order below approximately 20 K, and without thermal quenching the samples are mostly diamagnetic. As the high temperature susceptibility shows excess magnetization with respect to the spin-only value,[24] using formula units that are discussed below, we focus on investigating the nature of the ordered state. So, after thermally quenching to trap magnetic states, we probe the nuclear crystal structure at $T = 40$ K, where the sample is paramagnetic, and the magnetic structure at $T = 4$ K, where the sample shows magnetic order.

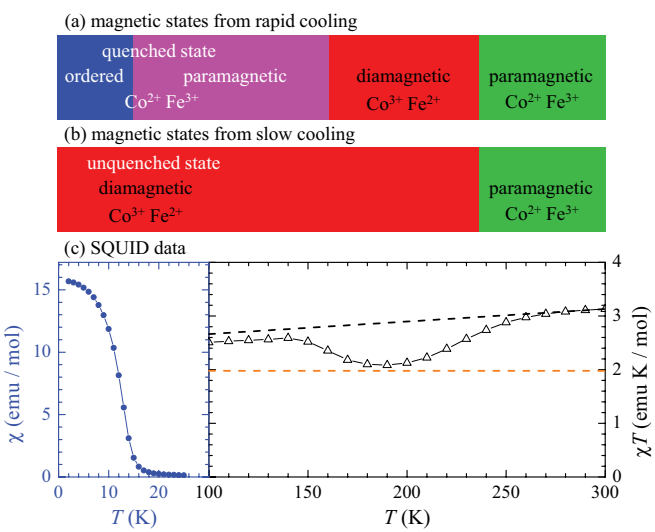

FIG. 2. (Color online) Magnetic phase transitions in Co-Fe. Following the temperature bar at the bottom of the figure, (a) a schematic of magnetic states upon warming Co-Fe after a quench achieved by dunking from room temperature into a cryogenic bath, (b) a schematic of magnetic states upon warming Co-Fe after a slow cool of less than 1 K/min to base temperature, and (c) the manifestation of these states as measured by a SQUID magnetometer. The magnetic susceptibility near the ordered state (blue circles) and in a field of 10 mT and the magnetic susceptibility, temperature product (open triangles) in a field of 1 T are shown as a function of warming the sample temperature in a quenched state. The spin-only calculated susceptibility (dotted orange line) and linearized high-temperature susceptibility (dotted black line) are also shown. Uncertainty bars are derived from longitudinal moment scans.

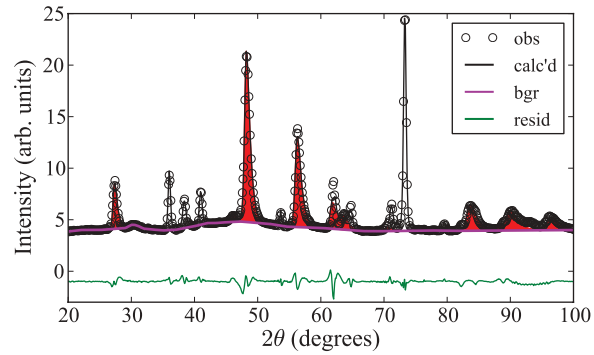

FIG. 3. (Color online) Neutron powder diffraction of Co-Fe at $T = 40$ K. Observed scattering is shown as open circles (obs), a full fit including sample mount contributions is shown as a black line (calc'd), the diffuse background is illustrated with a magenta line (bgr), and the residuals of the fit are shown below the zero line with a green line (resid). The signal due to Co-Fe is emphasized with a red filling. Experimental uncertainties derived from counting statistics are smaller than the plotting symbols.

The nuclear crystal structure of Co-Fe can be modeled with space group $Fm\bar{3}m$ (No. 225), where ferricyanide molecules and cobalt ions are alternately centered on the high symmetry points of the unit cell, with heavy water bound to cobalt when ferricyanide is absent, and potassium ions and heavy-water molecules filling in voids.[6,8,25] This structure is used as a starting point to fit the $T = 40$ K thermally quenched Co-Fe contribution to the measured intensity profile (Fig. 3), which also has sample mount contributions due to $P63/mmc$ (No. 194) D_2O and $Fm\bar{3}m$ (No. 225) aluminum.[26,27] Incomplete trapping of the high-temperature state by quenching in Co-Fe gives rise to a highly microstrained nuclear structure,[25] and to account for this effect during refinement we use an asymmetric double sigmoidal peak shape, namely

$$y_{a2s} = \frac{I}{2.49w}\left(1 - \frac{1}{1+e^{-\frac{\theta-\theta_c}{3.43w}}}\right)\left(\frac{1}{1+e^{-\frac{\theta-\theta_c}{w}}}\right), \quad (8)$$

where I is the intensity, w is the width, and θ_c is the center of the reflection, and these fits yield an effective lattice constant of 10.23 Å. Observed Co-Fe reflections that can be clearly separated from sample holder reflections are used to extract structure factors. In modeling the unit cell, the cobalt to iron ratio was determined with EDS, while the room temperature oxidation states are determined with FT-IR. The carbon and nitrogen content were established with combustion analysis, and the potassium ions provide charge balance. Finally, the

TABLE I. Atomic coordinates and occupancies for Co-Fe at $T = 40$ K.

Atom	Position	n	x	y	z
Co	4a	1	0.5	0.5	0.5
Fe	4b	0.73	0	0	0
C	24e	0.73	0.212	0	0
N	24e	0.73	0.313	0	0
K	8c	0.135	0.25	0.25	0.25
O	24e	0.27	0.243	0	0
D	96k	0.135	0.303	0.060	0.060

heavy-water concentration and positions were refined along with the scale factor to fit the structure factors.

To begin, refinement yielded interstitial heavy-water pseudoatoms at the $8c$ position ($n = 0.618$, $B = 5$) and the $32f$ position ($x = 0.3064$, $n = 0.333$, $B = 20$), after which all other parameters were fixed (Table I) and Fourier components of the heavy water were further refined to give the interstitial distribution shown in Fig. 1. These refinements give a chemical formula of $K_{0.27}Co[Fe(CN)_6]_{0.73}[D_2O_6]_{0.27}\cdot 1.42D_2O$. Moreover, at room temperature, the more complete chemical formula with oxidation states of the metal ions included is $K_{0.27}Co^{2+}_{0.94}Co^{3+}_{0.06}[Fe^{3+}(CN)_6]_{0.58}$ $[Fe^{2+}(CN)_6]_{0.15}$ $[D_2O_6]_{0.27}\cdot 1.42D_2O$, or more compactly represented by $Co^{2+}_{0.94}Co^{3+}_{0.06}Fe^{3+}_{0.58}Fe^{2+}_{0.15}$.

Having highly ionic wave functions, the magnetic ground states of Co and Fe in Co-Fe are well described with ligand field theory.[28] As displayed in Fig. 1, the iron atoms are octahedrally coordinated by carbon atoms that introduce a ligand field splitting parameter (Δ_{Fe}) of approximately 0.70 aJ (35 000 cm^{-1} or 4.3 eV), and typical Fe Racah parameters put d^5 Fe^{3+} into a $^2T_{2g}$ ground state, and d^6 Fe^{2+} into a diamagnetic $^1A_{1g}$ ground state. Similarly, cobalt atoms are octahedrally coordinated with oxygen and nitrogen atoms to give $\Delta_{Co^{3+}} \approx 0.46$ aJ (23 000 cm^{-1} or 2.9 eV) for d^6 Co^{3+} that has a diamagnetic $^1A_{1g}$ ground state, and $\Delta_{Co^{2+}} \approx 0.20$ aJ (10 000 cm^{-1} or 1.2 eV) for d^7 Co^{2+} that has a $^4T_{1g}$ ground state, using typical Co Racah parameters. At temperatures much less than the spin-orbit coupling energy, only the lowest energy total angular momentum levels are appreciably occupied, so that the relevant states are $Fe^{3+}[J = 1/2,\ g_J = (2 + 4k)/3,\ g_L = 4k/3,\ g_S = 2/3]$ and $Co^{2+}[J = 1/2,\ g_J = (10 + 2Ak)/3,\ g_L = 2Ak/3,\ g_S = 10/3]$, where A is expected to be nearly 1.5 due to the weak ligand field, and k is the orbital reduction parameter. It is worth noting that analogous orbitally degenerate terms have been observed for d^5 $Fe^{3+}(^2T_{2g})$ in $K_3Fe(CN)_6$,[29] and d^7 $Co^{2+}(^4T_{1g})$ in $K_{1.88}Co[Fe(CN)_6]_{0.97}\cdot 3.8H_2O$ and $Na_{1.52}K_{0.04}Co[Fe(CN)_6]_{0.89}\cdot 3.9H_2O$.[30] Alternatively, if interaction with the lattice drastically quenches the orbital moment, spin-orbit coupling no longer splits the ground states and the magnetic parameters become $Fe^{3+}[J = 1/2,\ g_J = 2,\ g_L = 0,\ g_S = 2]$ and $Co^{2+}[J = 3/2,\ g_J = 2,\ g_L = 0,\ g_S = 2]$. To estimate the relative proportion of the different oxidation states in the thermally quenched state, the effective paramagnetic moment is linearized as a function of temperature for the 300 and 100 K states,[31] and the measured lattice constant is compared to a weighted average of quenched and ground-state lattice constants,[16] to self-consistently give $Co^{2+}_{0.90}Co^{3+}_{0.10}Fe^{3+}_{0.54}Fe^{2+}_{0.19}$ for the magnetic quenched state at 100 K and below that is analyzed in detail herein.

Cooling the sample further, subsequent to quenching, the bulk magnetization measured in 10 mT showed the well-documented upturn at around 15 K corresponding to the onset of magnetic order (Fig. 2). Therefore, additional NPD was performed at 4 K in applied fields of 10 mT, 1 T, and 4 T (Fig. 4) to compare to the scattering in the paramagnetic state. Furthermore, polarized NPD was performed at 4 K in an applied field of 1 T [Fig. 4(d)], where the difference between diffractograms for up and down incident neutron polarizations increases signal to noise of the measured magnetic structure at reflections with large nuclear contributions. For each of the three experimental conditions where magnetic scattering is observed, we compare the results of eight plausible but different models that all have moments along the applied field. Specifically, each possible case considers various combinations of the parallel or antiparallel alignment of Co and Fe moments when each ion possesses either spin-only or orbitally

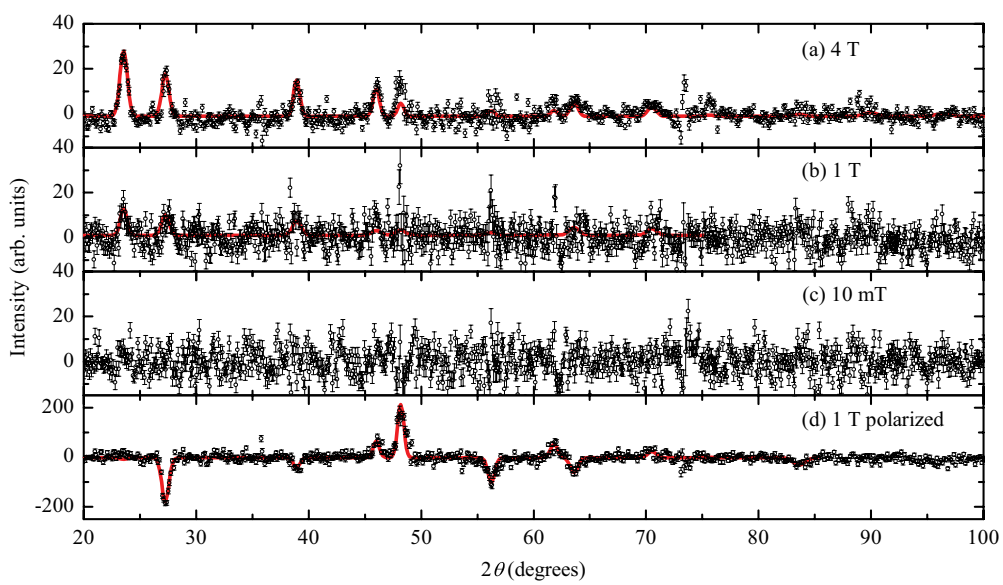

FIG. 4. (Color online) Magnetic neutron powder diffraction of Co-Fe at $T = 4$ K as a function of applied magnetic field. The difference between the $T = 40$ K diffractogram and the $T = 4$ K diffractogram (open circles) along with profile fits to intensities (red line from model 1 for 4 and 1 T data in Table II) are shown for (a) 4 T, (b) 1 T, and (c) 10 mT. Additionally, the difference between the $T = 4$ K up-neutron-polarization diffractogram and the $T = 4$ K down-neutron-polarization diffractogram (open circles) along with profile fits to intensity (red line from model 5 for polarized data in Table II) are shown for (d) 1 T. Uncertainty bars on experimental data points are statistical in nature representing one standard deviation from the mean, using counting statistics.

TABLE II. Comparison of the eight magnetic models, as described in the text, numbered 1–8 for Co-Fe at $T = 4$ K in different magnetic fields tabulated as "Cond.", which is shorthand for experimental condition, where "P" designates the data acquired with polarized neutrons. Here "Align." is short for "moment alignment," where $+$ denotes parallel alignment of moments and $-$ denotes antiparallel alignment of moments. The units of $m_{z,\mathrm{Co}}$ and $m_{z,\mathrm{Fe}}$ are μ_B, and the units of M are $\mu_B\,\mathrm{mol}^{-1}$. The sum of the residuals are normalized to model 1 for each experimental condition.

	Cond.	Align.	$g_{S,\mathrm{Co}}$	$g_{L,\mathrm{Co}}$	$g_{S,\mathrm{Fe}}$	$g_{L,\mathrm{Fe}}$	$J_{z,\mathrm{Co}}$	$J_{z,\mathrm{Fe}}$	$m_{z,\mathrm{Co}}$	$m_{z,\mathrm{Fe}}$	M	$\sum_j$ residual^2
1	4 T	+	10/3	1	2/3	4/3	0.63 ± 0.02	0.13 ± 0.03	2.7	0.3	2.6	1.000
2	4 T	−	10/3	1	2/3	4/3	0.62 ± 0.02	0.00 ± 0.02	2.7	0.0	2.4	1.019
3	4 T	+	10/3	1	2	0	0.64 ± 0.02	0.12 ± 0.04	2.8	0.2	2.6	1.000
4	4 T	−	10/3	1	2	0	0.63 ± 0.02	0.00 ± 0.11	2.7	0.0	2.5	1.020
5	4 T	+	2	0	2/3	4/3	1.08 ± 0.03	0.16 ± 0.03	2.2	0.3	2.1	1.028
6	4 T	−	2	0	2/3	4/3	1.04 ± 0.03	0.00 ± 0.03	2.1	0.0	1.9	1.049
7	4 T	+	2	0	2	0	1.09 ± 0.03	0.12 ± 0.04	2.2	0.2	2.1	1.030
8	4 T	−	2	0	2	0	1.05 ± 0.03	0.00 ± 0.03	2.1	0.0	1.9	1.048
1	1 T	+	10/3	1	2/3	4/3	0.37 ± 0.03	0.20 ± 0.09	1.6	0.4	1.7	1.000
2	1 T	−	10/3	1	2/3	4/3	0.37 ± 0.02	0.00 ± 0.04	1.6	0.0	1.4	1.020
3	1 T	+	10/3	1	2	0	0.38 ± 0.03	0.12 ± 0.07	1.6	0.2	1.6	1.004
4	1 T	−	10/3	1	2	0	0.38 ± 0.05	0.00 ± 0.11	1.6	0.0	1.5	1.019
5	1 T	+	2	0	2/3	4/3	0.64 ± 0.04	0.20 ± 0.09	1.3	0.4	1.4	1.001
6	1 T	−	2	0	2/3	4/3	0.64 ± 0.10	0.00 ± 0.21	1.3	0.0	1.2	1.022
7	1 T	+	2	0	2	0	0.65 ± 0.04	0.13 ± 0.07	1.3	0.3	1.3	1.006
8	1 T	−	2	0	2	0	0.63 ± 0.09	0.00 ± 0.08	1.3	0.0	1.1	1.021
1	P	+	10/3	1	2/3	4/3	0.38 ± 0.01	0.06 ± 0.02	1.6	0.1	1.5	1.000
2	P	−	10/3	1	2/3	4/3	0.40 ± 0.02	0.00 ± 0.01	1.7	0.0	1.5	1.058
3	P	+	10/3	1	2	0	0.36 ± 0.02	0.18 ± 0.05	1.6	0.4	1.6	1.004
4	P	−	10/3	1	2	0	0.40 ± 0.02	0.00 ± 0.02	1.7	0.0	1.5	1.065
5	P	+	2	0	2/3	4/3	0.68 ± 0.02	0.06 ± 0.02	1.4	0.1	1.3	0.995
6	P	−	2	0	2/3	4/3	0.71 ± 0.02	0.00 ± 0.02	1.4	0.0	1.3	1.058
7	P	+	2	0	2	0	0.66 ± 0.03	0.16 ± 0.06	1.3	0.3	1.3	1.005
8	P	−	2	0	2	0	0.74 ± 0.03	0.00 ± 0.05	1.5	0.0	1.3	1.079

degenerate magnetic states (Table II). The analyses indicate that most magnetism resides on the Co 4a site for all models, with a parallel alignment of Fe and Co moments giving the best fits and χ^2 surfaces suggesting a reduced but present orbital moment on both ions. No magnetic scattering is observed in 10 mT, and increased coherent magnetic scattering appears with increasing field, which is consistent with the presence of significant random anisotropy, where a correlated spin glass (CSG) is the ground state and sufficiently large fields cause entrance into a ferromagnetic phase with wandering axis (FWA) state or at even larger fields a nearly collinear (NC) state.[32]

Analytical expressions for the magnetization process for magnets with random anisotropy are available[32] for the Hamiltonian

$$\mathcal{H} = -\mathcal{J}\sum_{i,j} S_i \cdot S_j - D_r \sum_i (\hat{n}_i \cdot S_i)^2 - D_c \sum_i \left(S_i^z\right)^2 - g\mu_B \sum_i H \cdot S_i, \tag{9}$$

where $\mathcal{J}$ is the superexchange constant, S is the spin operator, D_r is strength of the random anisotropy, $\hat{n}$ is the direction of the random on-site anisotropy, D_c is the strength of the coherent anisotropy, g is the Landé factor, and H is the applied field. In the FWA regime where the applied field energy is larger than the random anisotropy energy but much less than the exchange field, the low-temperature magnetization is

$$M_{\mathrm{FWA}} = M_S - \frac{6\sqrt{2}D_r^2\Omega M_S}{5\pi^2 a^3 (z\mathcal{J})^{3/2}(H+H_C)^{1/2}} = M_S\left[1 - \frac{D_{\mathrm{FWA}}^{1/2}}{(H+H_C)^{1/2}}\right], \tag{10}$$

where M_S is the saturation magnetization, Ω is the integrated local anisotropy correlation function, z is the number of magnetic neighbors, a is the mean distance between neighboring spin sites, H_C is the coherent anisotropy field, and D_{FWA} is a measure of the random anisotropy to superexchange strengths. For the NC phase that is reached when the applied field and coherent anisotropy field are much larger than the exchange field, the low-temperature magnetization is

$$M_{\mathrm{NC}} = M_S - \frac{4D_r^2 M_S}{15a^6(H+H_C)^2} = M_S\left[\frac{1 - D_{\mathrm{NC}}^2}{(H+H_C)^2}\right], \tag{11}$$

where D_{NC} is a measure of the random anisotropy. Based upon the magnetic ordering temperature, Co-Fe is expected to be in an FWA-like phase, and although both FWA and NC expressions may be fit to the low-temperature magnetization data (Fig. 5), the parameters extracted by the NC fit are not consistent with the derivation limit for Eq. (11), further suggesting an FWA-like state.

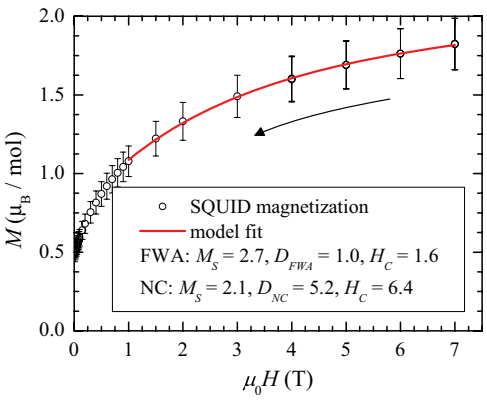

FIG. 5. (Color online) SQUID magnetization of Co-Fe at $T = 2$ K. Experimental magnetization is shown as open circles (SQUID magnetization) and model fits as a red line (model fit), where FWA and NC are visually indistinguishable; $M(1\text{ T}) = 1.1 \pm 0.1\ \mu_B\ \text{mol}^{-1}$ and $M(4\text{ T}) = 1.6 \pm 0.2\ \mu_B\ \text{mol}^{-1}$. The units of M_S are $\mu_B\ \text{mol}^{-1}$, and H_C, D_{FWA}, and D_{NC} are all units of Tesla. Uncertainty bars represent one standard deviation from the mean, where statistics are generated by measuring the magnetization of the 14 synthesis batches required to generate 4.37 g for NPD.

IV. DISCUSSION

We have presented neutron diffraction and bulk magnetization measurements of $K_{0.27}Co[Fe(CN)_6]_{0.73}[D_2O_6]_{0.27}\cdot 1.42D_2O$ that suggest a CSG ground state that enters a FWA-like state in applied magnetic fields of the order 1 T and larger (Fig. 6). This conclusion is based upon the field dependence of the magnetization, and particularly the diffraction experiments that show an absence of long-range order in the 10 mT data and ordered moments that are induced by the applied field, ruling out a high-field domain magnetization process. This random-anisotropy-based magnetization process explains the appreciable slope observed for Co-Fe even in fields of 7 T at 2 K (Fig. 4), in a way similar to the magnetization process at low temperature and high-magnetic fields for the vanadium tetracyanoethylene molecular magnet prepared using solvent based methods.[33] This magnetization process is different than for other reported cubic complex cyanide systems that have magnetically ordered ground states and saturated magnetizations at 2 K and 7 T.[12–14] The high field behavior in Co-Fe is not restricted to the thermally quenched state, but is also present in "stable" Co-Fe and photoinduced Co-Fe.[31] The CSG ground state is consistent with previous ac-susceptibility measurements of $K_{1-2x}Co_{1+x}[Fe(CN)_6]\cdot yH_2O$ $(0.2 \leqslant x \leqslant 0.4,\ \ y \approx 5)$ that showed glassy behavior,[3] although the relative orientation we find for Co and Fe at 1 T is contrary to the XMCD experiment that reported antiparallel Co and Fe at 1 T in $Rb_{1.8}Co_4[Fe(CN)_6]_{3.3}\cdot 13H_2O$ and $K_{0.1}Co_4[Fe(CN)_6]_{2.7}\cdot 18H_2O$.[4] For fields of 1 and 4 T we find a parallel alignment of Co and Fe moments minimizes the residuals between model and data, and this alignment is clearly seen for the low-angle 4 T peaks (Fig. 7). However, the lack of coherent scattering for CSG means we cannot strictly discuss the nature of the superexchange interaction in the ground state, although we infer some significant ferromagnetic character based upon the high-field regime. One must also be careful about applying qualitative Goodenough-Kanamori rules to this system,[36–38] as the single-electron states are not only mixed from electrostatic interactions, but also due to the aforementioned presence of spin-orbit coupling. Nevertheless, within the single-electron state picture, Co-Fe has two ferromagnetic (t_{2g}-e_g) exchange paths and one antiferromagnetic (t_{2g}-t_{2g}) exchange path, with antiferromagnetic paths typically being stronger than ferromagnetic in addition to having a strong dependence upon

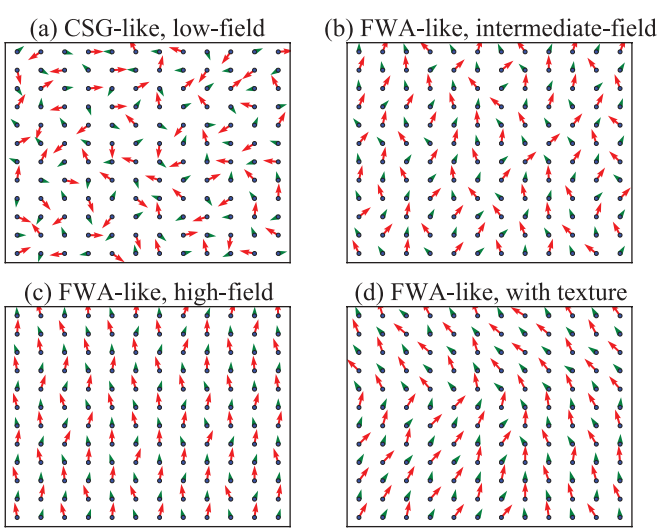

FIG. 6. (Color online) An illustration of magnetic structure for different magnetic field regimes. Here the magnetic field points towards the top of the page, short arrows represent iron moments, and long arrows represent cobalt moments. (a) The Co-Fe sample cooled in zero field has a CSG-like state with no average on-site moment, as shown for the measurement of magnetic scattering in 10 mT [Fig. 3(c)]. (b) The application of magnetic field cants the moments towards the field [Figs. 3(b) and 3(d)], and (c) larger fields induce larger average moments [Fig. 3(a)]. (d) More complicated mesoscopic states that contain texture are also possible, but are not unambiguously determined with our data.

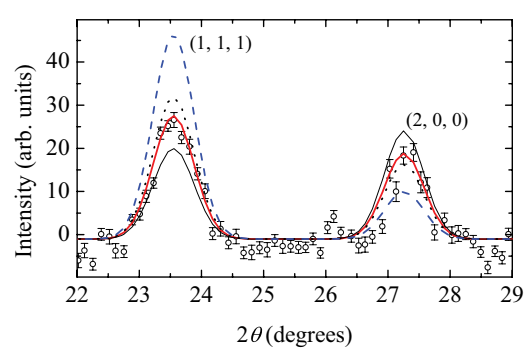

FIG. 7. (Color online) Visual comparison of magnetic configurations for Co-Fe. Here the low angle $H = 4$ T data (open circles) are set side by side with model 1 for 4 T from Table II (thick solid, red line), model 2 for 4 T from Table II (dotted, black line), a ferrimagnetic structure with a 3:1 Co:Fe spin ratio (dashed, blue line), and a ferromagnetic structure with a 3:1 Co:Fe spin ratio (thin solid, black line). Uncertainty bars are representative of one standard deviation from the mean, using counting statistics.

distance and bond angle. As such, small changes in sample preparation and microstrain may affect the average coupling in Co-Fe Prussian blue analog systems and also be related to the glassy magnetic order. A band structure calculation using a full potential linearized augmented plane wave method resulted in an antiferromagnetic ground state for Co-Fe, with $+0.296\ \mu_B$ on the Co site and $-0.280\ \mu_B$ on the Fe site,[39] although such values do not agree with experimental findings.

For the Co-Fe presented, care was taken to ensure that the average particle size was greater than ≈100 nm (as measured by TEM) to avoid finite size effects,[34] and the FWA-like phase can explain the previously reported changes in low-temperature high-field magnetization with particle size as a tuning of the local random anisotropy with size, whereby larger particles require higher fields to saturate at base temperature because they are deeper in a glassy phase. The saturation value for bulk $K_{0.27}Co[Fe(CN)_6]_{0.73}[D_2O_6]_{0.27}\cdot 1.42D_2O$, $M_S = 2.7 \pm 0.3\ \mu_B\ \mathrm{mol}^{-1}$, is comparable to a variety of similar states with different degrees of orbital reduction on Co and Fe sites; for example, considering complete orbital moments on both Co and Fe gives $M_S \approx 2.5\ \mu_B\ \mathrm{mol}^{-1}$ and spin-only moments gives $M_S \approx 3.2\ \mu_B\ \mathrm{mol}^{-1}$.

The NPD experiments show a model-independent increase in coherent magnetic scattering as a function of field, and a slightly form-factor dependent ratio of Co to Fe moments (Table II). A parallel alignment of Co and Fe is found for both 1 and 4 T, and when an antiparallel alignment is forced, Fe moments go to zero to achieve best fits. The moment ratio is heavily dictated by the low-Q peaks where the form factor has little effect, while the scale of the moments is different depending upon the presumed shape of the scatterer. Previous neutron diffraction measurements have shown covalency effects, due to σ bonding and π backbonding with CN, to be important in the chemically similar $CsK_2[Fe(CN)_6]$.[35] Covalency can increase the direct-space size of the moments, thereby decreasing the reciprocal-space size even in the presence of orbital moments. For Co-Fe, the smaller reciprocal-space form factors give magnetizations most similar to those determined by SQUID magnetometry, although covalency makes assignment of orbital and spin magnetism based upon spatial distribution inconclusive. We do not refine the form factor in this paper because high parameter covariance is introduced. Finally, small quantitative differences between SQUID and NPD moment values may also be due to sample inhomogeneity overestimating the NPD moments, and unitemized experimental uncertainties due to the complicated and highly unstoichiometric formulation of the Co-Fe material, but our conclusions remain robust with respect to such perturbations. The linewidths for magnetic and nuclear NPD are similar, suggesting comparable domain sizes for the scattering objects, but it is possible that the induced moments have a texture over some other length scale [Fig. 5(d)], a possibility suggested by cluster-glass behavior in ac-susceptibility studies.[3] As shown in the Appendix, regions of coherent magnetization at an angle ξ from the applied field would rescale the measured NPD longitudinal moment by $\cos\xi\sqrt{\frac{2}{\cos^2\xi+1}}$, but the similarity between the polarized and unpolarized magnetic diffraction further suggests that such an effect is small in our samples.

V. CONCLUSIONS

The neutron diffraction and bulk magnetization measurements of Co-Fe suggest a magnetization process that evolves from a correlated spin glass to a quasiferromagnetic state with increasing magnetic field, where average Co and Fe moments are induced to lie along the applied field. These results are interpreted within the specific limits of temperature, magnetic field, and sample preparation used, but are suggestive to the nature of other Co-Fe systems that include cation-free and photoinduced samples, which may warrant similar studies. Ultimately, when considering memory storage applications of molecule based magnetic materials, structure-property relationships that may give rise to coherent and random anisotropy will be important to consider.

ACKNOWLEDGMENTS

D.M.P. acknowledges support from the NRC/NIST postdoctoral associateship program. Research at High Flux Isotope Reactor at ORNL was sponsored by the Scientific User Facilities Division, Office of Basic Energy Sciences, US Department of Energy. This work was supported, in part, by NSERC, CFI, and NSF through Grants No. DMR-1005581 (D.R.T.) and No. DMR-0701400 and No. DMR-1202033 (M.W.M.).

APPENDIX: EFFECT OF CANTING ON INTENSITY

A powder sample consisting of domains canted at an angle ξ away from the applied field, with random rotational distribution, may give the same unpolarized NPD signal as domains along the field, but with a different magnetic moment. With the magnetic field along the z axis, and the scattering vector along the x axis, the uncanted magnetic moment is simply

$$\mathbf{M_u} = (0,0,M), \tag{A1}$$

and the canted moment can be expressed as

$$\mathbf{M_{canted}} = M(\sin\xi\cos\phi, \sin\xi\sin\phi, \cos\xi), \tag{A2}$$

where ξ is the canting angle, ϕ is the rotation angle about the field, and M is the magnitude of the magnetic moment. The interaction vector[21]

$$|\mathbf{M}_\perp|^2 = \sum_{\alpha,\beta}(\delta_{\alpha\beta} - \widehat{Q}_\alpha\widehat{Q}_\beta)M_\alpha^* M_\beta \tag{A3}$$

then gives a dependence of the intensity on the canting angle such that

$$|\mathbf{M_{u,\perp}}|^2 = M^2 \tag{A4}$$

and

$$|\mathbf{M_{canted,\perp}}|^2 = M^2\frac{\cos^2\xi + 1}{2}, \tag{A5}$$

where random ϕ angles have been averaged over. Therefore, an uncanted model with a z component (relevant to compare with longitudinal magnetization) of M can give the same unpolarized NPD intensity as a canted model with a z component of $M\cos\xi\sqrt{\frac{2}{\cos^2\xi+1}}$.

[1]O. Sato, T. Iyoda, A. Fujishima, and K. Hashimoto, Science **272**, 704 (1996).
[2]O. Sato, Y. Einaga, A. Fujishima, and K. Hashimoto, Inorg. Chem. **38**, 4405 (1999).
[3]D. A. Pejaković, C. Kitamura, J. S. Miller, and A. J. Epstein, Phys. Rev. Lett. **88**, 057202 (2002).
[4]G. Champion, V. Escax, C. C. dit Moulin, A. Bleuzen, and M. Verdaguer, J. Am. Chem. Soc. **123**, 12544 (2001).
[5]Z. Salman, T. J. Parolin, K. H. Chow, T. A. Keeler, R. I. Miller, D. Wang, and W. A. MacFarlane, Phys. Rev. B **73**, 174427 (2006).
[6]F. Herren, P. Fischer, A. Ludi, and W. Hälg, Inorg. Chem. **19**, 956 (1980).
[7]P. Day, F. Herren, A. Ludi, H. U. Güdel, F. Hulliger, and D. Givord, Helv. Chim. Acta **63**, 148 (1980).
[8]H. J. Buser, D. Schwarzenbach, W. Petter, and A. Ludi, Inorg. Chem. **16**, 2704 (1977).
[9]M. R. Hartman, V. K. Peterson, Y. Liu, S. S. Kaye, and J. R. Long, Chem. Mater. **18**, 3221 (2006).
[10]S. Adak, L. L. Daemen, and H. Nakotte, J. Phys. Conf. Ser. **251**, 012007 (2010).
[11]A. Kumar, S. M. Yusuf, L. Keller, and J. V. Yakhmi, Phys. Rev. Lett. **101**, 207206 (2008).
[12]A. Kumar, S. M. Yusuf, and L. Keller, Phys. Rev. B **71**, 054414 (2005).
[13]A. Kumar and S. M. Yusuf, Pramana J. Phys. **63**, 239 (2004).
[14]M. Mihalik, V. Kavečanský, S. Mataš, M. Zentková, O. Prokhenko, and G. André, J. Phys. Conf. Ser. **200**, 022035 (2010).
[15]J.-H. Park, F. Frye, N. E. Anderson, D. M. Pajerowski, Y. D. Huh, D. R. Talham, and M. W. Meisel, J. Magn. Magn. Mater. **310**, 1458 (2007).
[16]C. Chong, M. Itoi, K. Boukheddaden, E. Codjovi, A. Rotaru, F. Varret, F. A. Frye, D. R. Talham, I. Maurin, D. Chernyshov, and M. Castro, Phys. Rev. B **84**, 144102 (2011).
[17]Certain commercial equipment, instruments, or materials are identified in this paper to foster understanding. Such identification does not imply recommendation or endorsement by the National Institute of Standards and Technology, nor does it imply that the materials or equipment identified are necessarily the best available for the purpose.
[18]V. O. Garlea, B. C. Chakoumakos, S. A. More, G. B. Taylor, T. Chae, R. G. Maples, R. A. Riedel, G. W. Lynn, and D. L. Shelby, Appl. Phys. A **99**, 531 (2010).
[19]E. Lelièvre-Berna, A. S. Wills, E. Bourgeat-Lami, A. Dee, T. Hansen, P. F. Henry, A. Poole, M. Thomas, X. Tonon, J. Torregrossa, K. H. Andersen, F. Bordenave, D. Jullien, P. Mouveau, B. Guérard, and G. Manzin, Meas. Sci. Technol. **21**, 055106 (2010).
[20]A. S. Wills, E. Lelièvre-Berna, F. Tasset, J. Schweizer, and R. Ballou, Physica B **356**, 254 (2005).
[21]J. Schweizer, *Neutron Scattering from Magnetic Materials*, edited by T. Chatterji (Elsevier, New York, 2006).
[22]J. J. Sakurai, *Modern Quantum Mechanics*, edited by S. F. Tuan (Addison-Wesley, Reading, MA, 1994).
[23]E. Clementi and C. Roetti, At. Data Nucl. Data Tables **14**, 177 (1974).
[24]The spin-only χT for this Co-Fe sample is calculated using Curie's law for d^7 $Co^{2+}_{0.94}$ $[S = 3/2]$, which gives $\chi T_{\text{Co spin}} = 0.94$ Co^{2+}/mol$\times$1.876 emu K/Co^{2+} = 1.763 emu K/mol, and d^5 $Fe^{3+}_{0.58}$ $[S = 1/2]$, which gives $\chi T_{\text{Fe spin}} = 0.58$ Fe^{3+}/mol $\times$ 0.375 emu K/Fe^{3+} = 0.218 emu K/mol, to yield $\chi T_{\text{Co-Fe spin}} = 1.981$ emu K/mol.
[25]M. Hanawa, Y. Moritomo, A. Kuriki, J. Tateishi, K. Kato, M. Takata, and M. Sakata, J. Phys. Soc. Jpn. **72**, 987 (2003).
[26]L. G. Dowell and A. P. Rinfret, Nature (London) **188**, 1144 (1960).
[27]A. W. Hull, Phys. Rev. **10**, 661 (1917).
[28]B. N. Figgis and M. A. Hitchman, *Ligand Field Theory and Its Applications* (Wiley-VCH, Berlin, 2000).
[29]B. N. Figgis, M. Gerloch, and R. Mason, Proc. R. Soc. London Ser. A **309**, 91 (1969).
[30]T. Matsuda, K. Jungeun, and M. Yutaka, J. Am. Chem. Soc. **132**, 12206 (2010).
[31]D. M. Pajerowski, Ph.D. Dissertation, University of Florida, Gainesville, FL, 2010.
[32]E. M. Chudnovsky, W. M. Saslow, and R. A. Serota, Phys. Rev. B **33**, 251 (1986).
[33]P. Zhou, B. G. Morin, J. S. Miller, and A. J. Epstein, Phys. Rev. B **48**, 1325 (1993).
[34]D. M. Pajerowski, F. A. Frye, D. R. Talham, and M. W. Meisel, New J. Phys. **9**, 222 (2007).
[35]B. N. Figgis, E. S. Kucharski, J. M. Raynes, and P. A. Reynolds, J. Chem. Soc. Dalton Trans. **1990**, 3597 (1990).
[36]J. B. Goodenough, Phys. Rev. **100**, 564 (1955).
[37]J. B. Goodenough, J. Phys. Chem. Solids **6**, 287 (1958).
[38]J. Kanamori, J. Phys. Chem. Solids **10**, 87 (1959).
[39]K. Takegahara and H. Harima, Phase Trans. **75**, 799 (2002).